IOP Publishing Smart Materials and Structures
Smart Mater. Struct. 26 (2017) 085043 (12pp) https://doi.org/10.1088/1361-665X/aa75f7

# Robust control of dielectric elastomer diaphragm actuator for human pulse signal tracking

**Zhihang Ye[1], Zheng Chen[1,4], Ramazan Asmatulu[2] and Hoyin Chan[3]**

[1] Department of Electrical Engineering and Computer Science, Wichita State University, 1845 Fairmount St., Wichita, KS 67260-0083, United States of America
[2] Department of Mechanical Engineering, Wichita State University, 1845 Fairmount St., Wichita, KS 67260-0133, United States of America
[3] Department of Mechanical and Biomedical Engineering, City University of Hong Kong, 83 Tat Chee Avenue, Kowloon Tong, Hong Kong

E-mail: zheng.chen@wichita.edu

Received 3 January 2017, revised 15 May 2017
Accepted for publication 31 May 2017
Published 28 July 2017

**Abstract**

Human pulse signal tracking is an emerging technology that is needed in traditional Chinese medicine. However, soft actuation with multi-frequency tracking capability is needed for tracking human pulse signal. Dielectric elastomer (DE) is one type of soft actuating that has great potential in human pulse signal tracking. In this paper, a DE diaphragm actuator was designed and fabricated to track human pulse pressure signal. A physics-based and control-oriented model has been developed to capture the dynamic behavior of DE diaphragm actuator. Using the physical model, an H-infinity robust control was designed for the actuator to reject high-frequency sensing noises and disturbances. The robust control was then implemented in real-time to track a multi-frequency signal, which verified the tracking capability and robustness of the control system. In the human pulse signal tracking test, a human pulse signal was measured at the City University of Hong Kong and then was tracked using DE actuator at Wichita State University in the US. Experimental results have verified that the DE actuator with its robust control is capable of tracking human pulse signal.

Keywords: dielectric elastomer, robust control, human pulse signal tracking

(Some figures may appear in colour only in the online journal)

## 1. Introduction

Telediagnosis is an emerging research area that has attracted considerable attention. With the help of telediagnosis technologies, patients are able to receive medical services at home, be pre-screened before they reach a hospital, or even get early warnings before emergency situations occur [1–6]. Although transmission of images, sounds, and key physical data is widely used in telediagnosis processes, what is lacking is an effective method to transform real-time and sensitive information, which is needed for accurate diagnosis, such as tactile and olfactory information. For example, a traditional Chinese medical doctor needs to touch the wrist of a patient and feel the patient's pulse signal in order to diagnose a disease [7]. In order to record human pulse for traditional Chinese medicine diagnosis, a medical device located at the doctor's site is needed to replicate the pulse signal that is measured at the patient's site. The measuring of pulse pressure was successful [8]; however, how to track the measured pulse is still challenging since the biological tissue's compliant movement can not be well replicated by traditional electric motors. Hence, a soft actuator, which is capable of generating compliant movement and tracking a multi-frequency signal precisely, is needed for restoring the pulse movement from recorded human pulse data.

[4] Member, IEEE.

 

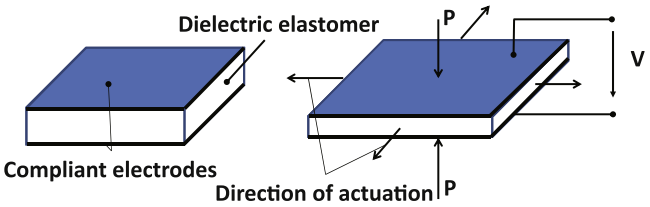


**Figure 1.** Illustration of dielectric elastomer actuator.

Dielectric elastomer (DE) has promising applications in biomedical applications due to its compliance. Pelrine *et al* studied many smart materials and electro-magnetic actuators in terms of energy density (energy per unit mass or unit volume) [9]. They found that electroactive polymer has an ideal energy density, which is very close to that of human muscles and about eight times greater than that of electro-magnetic actuator [9]. These ideal features make DE promising in developing new types of actuators for biomedical applications [10], which have great potential to overcome the drawbacks of traditional electric motors, such as a rigid structure, low energy efficiency, and heavy mass. A DE actuator usually consists of a DE membrane, which can be fabricated with a 3M VHB tape or silicone rubber. Two compliant electrodes made from conductive powder or grease are coated on both sides of the membrane. When a high voltage is applied, the electric charges between the two electrodes will cause the membrane to contract in its thickness direction. After removal of the driving voltage, the membrane will recover to its original thickness due to its internal stress [11]. Figure 1 illustrates the DE membrane's working principle.

Dielectric elastomers are capable of performing more than 100% strain under certain working conditions [12]. Many researchers have spent intensive effort on DE actuators, from theoretical modeling to analysis of DE materials [11, 13]. Ye *et al* have developed an artificial muscle and tendon structure using DE material and carbon fibers [14–16], and they investigated nano coating technology for DE material [17]. The unique features of DE material make it possible to use them in different fields. For robotics research purposes, with an additional supporting frame and mechanical components, diamond-shape and bow-tie-shape actuators were created [18–20], which are more suitable for practical purposes. In most of the applications of using DE material as actuator, the control system design is critical to achieve satisfactory positioning and tracking performances. Some work was focused on integrated sensing feedback control of DE actuators [21] and other work was focused on positioning control of DE actuators [22–24]. However, little work has been reported on robust trajectory tracking control for DE actuators.

In this paper, a DE diaphragm actuator was developed to track a human pulse signal. An H-infinity robust control was designed for the DE actuator to achieve robust and accurate trajectory tracking. A systematic approach was developed to design the H-infinity control, including physical modeling and internal stability analysis. To identify the dynamic model, the actuator was excited by applying a series of signals with different frequencies. A nominal transfer function was used to capture the dynamics of the actuator and the modeling error was bounded by another transfer function that represents the system's additive uncertainty. The H-infinity controller was designed based on the nominal transfer function. Based on the small gain theory, the H-infinity control system has proven internally stable, considering the bounded model uncertainty. With the H-infinity controller, the DE diaphragm actuator was able to track a multi-frequency signal with sensing noises and unknown disturbances, which verified the robustness and tracking capability of the control system. In the human pulse signal tracking test, a human pulse pressure signal was measured at the City University of Hong Kong, sent to Wichita State University (WSU) through the Internet, and then replicated by the DE actuator at WSU. Experimental results have shown that the DE diaphragm actuator was capable of tracking the human pulse pressure signal.

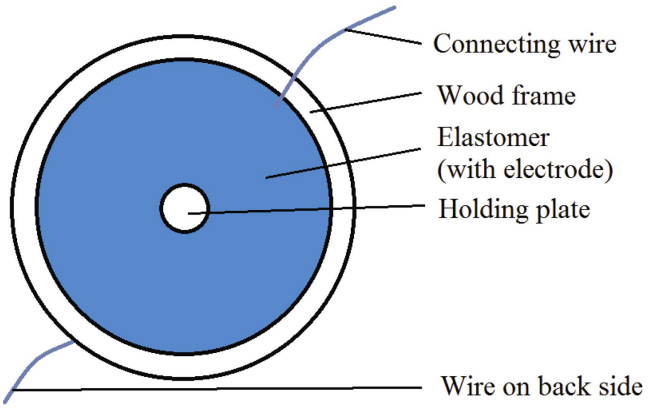


**Figure 2.** Design of diaphragm actuator.

The rest of this paper is organized as follows. Fabrication of the DE diaphragm actuator is described in section 2. Section 3 shows how to obtain the physical model, identify the model based on the frequency response, and estimate the model uncertainty. H-infinity control design is described in section 4. Experimental results on multi-frequency signal tracking and human pulse signal tracking are presented in section 5. Conclusions and future work are discussed in section 6.

## 2. Fabrication of diaphragm actuator

The chosen material and fabrication method were adjusted from former research work [15–17]. The design of the diaphragm actuator is shown in figure 2. A 1.5875 mm thick, 152.4 × 152.4 mm birch-wood plate was used for making a wood frame. 3M VHB-4910 tape was selected as the DE material. Graphite powder (Hillman Inc.) was selected as material for the compliant electrodes, since the dry graphite electrodes could sustain many actuation cycles and long storing time, which is good enough for experimental purposes.

The radius from the center of the diaphragm to its inner edge was 68.58 mm. After that, all needed components were cut from the birch-wood plate using an Epilog Laser Fusion

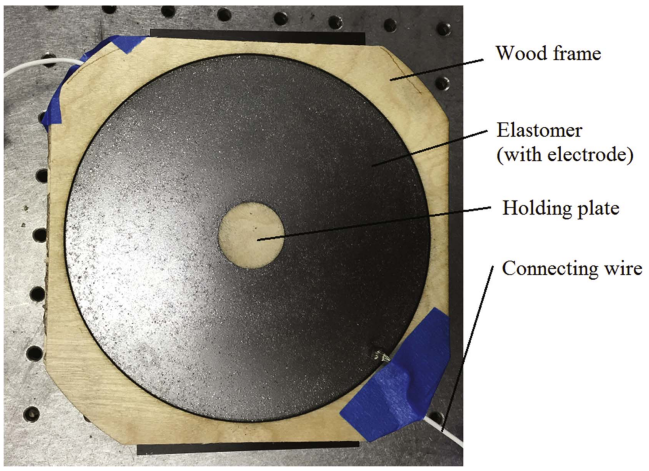


**Figure 3.** Fabricated diaphragm actuator.

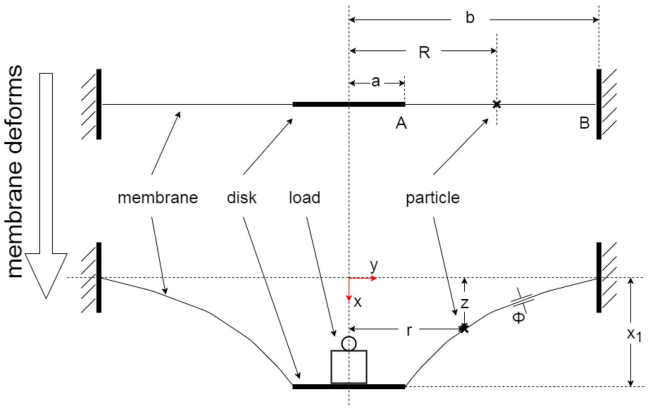


**Figure 4.** A sketch of a deformed diaphragm actuator.

cutter system. Then a 76.2 × 76.2 mm strip of VHB-4910 tape was attached with a circled horse pipe. By rolling the horse pipe, the tape was stretched by 100% uniformly in plane. Then the tape was fixed on the wood frame under a pre-stretched state. Two covering plates were attached in the same way at the center of the membrane. After the rigid components were firmly fixed on the VHB tape, the excessive VHB tape outside the frame was cut off. Since the central area of the elastomer membrane was not coated by compliant electrodes, a rigid plate for supporting the weight load was placed in the center of the actuator, and the radius of the covering plate was 12.7 mm. Graphite powder was then pasted on both sides of the uncovered area of the elastomer membrane, in order to make compliant and conductive electrodes. Copper fibers were simply attached on the electrodes to form the electrical connection. Figure 3 shows the diaphragm actuator ready for testing.

With this design, the small rigid plate was used to hold the weight load. The actuator itself was held horizontally by the outer edges of its frame in order to let the central plate move vertically. When a calibration weight was placed on the covering plate, the diaphragm actuator was able to deform downwards to a position that balanced the gravity of the weight load. Then a driving voltage was applied to the diaphragm. The Maxwell stress between the actuator's electrodes changed the DE's internal stress balance and forced the elastomer to deform so that the actuator lowered the weight load's position to a new balanced state. When the driving voltage was removed, the load returned to its original balanced position. For the safety concern, the upper side of the actuator was always grounded, and the other side was connected to a high voltage amplifier, which was contained in a small box to allow the actuator moving freely.

## 3. Modeling and identification of DE diaphragm actuator

A practical and reliable model is greatly needed in robust control design [25]. Suo *et al* have developed a physical model for a DE actuator, which is mainly described in partial differential equations (PDEs) [11, 14]. Figure 4 is showing how a diaphragm actuator deforms.

The figure is the sectional view of the actuator. Here set the center as original point, $x$ axis is pointing downward, and $y$ axis is pointing to the right. Before the elastomer membrane deforms, mark a particle in the membrane, the distance between the particle and the center of the diaphragm is $R$. Point $A$ is the inner edge of the membrane, which has a distance of $a$ to the central axis. Similarly, point $B$ is the outer edge, and the distance between $B$ and central axis is $b$. After put a weight load on the disk, the membrane deforms, and the particle moves to a new position. Its new position has a distance of $z$ below the plane of the un-deformed membrane, and a distance of $r$ to the central axis of the actuator. Because this actuator is axial symmetry, it only needs a sectional figure to fully describe the membrane's shape. Suo *et al* developed the model for the membrane's shape as following PDEs and a algebraic equation [14].

$$\frac{\mathrm{d}r}{\mathrm{d}R} = \lambda_1 \cos(\theta), \tag{1}$$

$$\frac{\mathrm{d}\theta}{\mathrm{d}R} = -\frac{s_2}{s_1 R}\sin(\theta), \tag{2}$$

$$\left[1 - \left(\frac{\Phi r}{R}\right)^2\right]\lambda_1^4 - \frac{mg}{R\sin\theta}\lambda_1^3 - \left(\frac{R}{r}\right)^2 = 0. \tag{3}$$

These equations fully describes three functions: $r(R)$, $\theta(R)$, and $\lambda_1(R)$, where $\lambda_1$ is the longitudinal stretches, $\theta$ is the slope connecting two particles, $s_1$ is the nominal longitudinal stress, $s_2$ is the nominal latitudinal stress, $\Phi$ is the voltage applied on the membrane, $m$ is the mass of load, and $g$ is gravitational acceleration. The boundary conditions are $r(A) = a$, and $r(B) = b$, where $A$ and $B$ are the distances from the membrane's inner edge and outer edge to the disk's center, when the membrane is un-deformed, $a$ and $b$ are the membrane's inner and outer radius, respectively. This model is used for static cases. When the load is moving, it is needed to consider the three functions $r(R)$, $\theta(R)$, and $\lambda_1(R)$ also as function of time. So use a variable $x_1$ to denote the movement of the disk, here the shape related functions are rewritten as $r(R, t)$, $\theta(R, t)$, and $\lambda_1(R, t)$, then the algebraic equation can

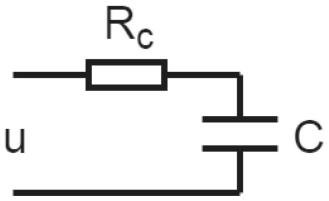


**Figure 5.** The circuit model of the diaphragm.

be rewritten as following equation.

$$\ddot{x}_1 = \frac{1}{m}\left(R\sin(\theta)\left(1 - \left(\frac{\Phi r}{R}\right)^2\right)\lambda_1 - \left(\frac{R}{r}\right)^2 \frac{R\sin(\theta)}{\lambda_1^3}\right), \quad (4)$$

where $\ddot{x}_1$ is the acceleration of the disk. Let $x_2 = \dot{x}_1$, then $\dot{x}_1 = \dot{x}_2$, together with the previous PDEs, a state space model can be formed to show the membrane's shape and the dynamics of the disk.

$$\begin{cases} \frac{\mathrm{d}r}{\mathrm{d}R} = \lambda_1\cos(\theta) \\ \frac{\mathrm{d}\theta}{\mathrm{d}R} = -\frac{s_2}{s_1 R}\sin(\theta) \\ \dot{x}_1 = x_2 \\ \dot{x}_2 = \frac{1}{m}\left(R\sin(\theta)\left(1 - \left(\frac{\Phi r}{R}\right)^2\right)\lambda_1 \right. \\ \left. - \left(\frac{R}{r}\right)^2 \frac{R\sin(\theta)}{\lambda_1^3}\right) \end{cases}. \quad (5)$$

The system is driven by the voltage applied on the membrane surface. Assuming the actuator's circuit structure can be equivalent to a classic resistor-capacitor (RC) circuit, which is showing in figure 5.

Then the relationship between the input voltage $u$ and voltage on the membrane surface $\Phi$ can be presented as following equation.

$$\dot{\Phi} = -\frac{1}{R_c C}\Phi - \frac{1}{R_c C}u, \quad (6)$$

where $R_c$ is the resistance, and $C$ denotes the actuator's capacitance. Let $\Phi = x_3$, together with the previous state space equations, the full model is as following equations.

$$\begin{cases} \frac{\mathrm{d}r}{\mathrm{d}R} = \lambda_1\cos(\theta) \\ \frac{\mathrm{d}\theta}{\mathrm{d}R} = -\frac{s_2}{s_1 R}\sin(\theta) \\ \dot{x}_1 = x_2 \\ \dot{x}_2 = \frac{1}{m}\left(R\sin(\theta)\left(1 - \left(\frac{x_3 r}{R}\right)^2\right)\lambda_1 \right. \\ \left. - \left(\frac{R}{r}\right)^2 \frac{R\sin(\theta)}{\lambda_1^3}\right) \\ \dot{x}_3 = -\frac{1}{R_c C}x_3 + \frac{1}{R_c C}u \end{cases}. \quad (7)$$

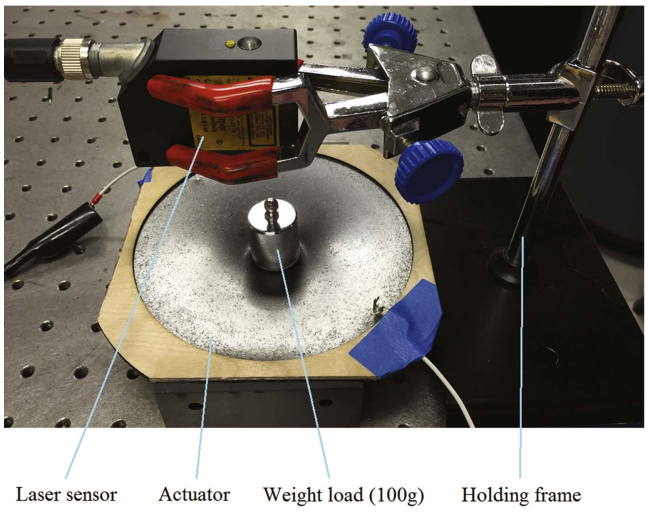


**Figure 6.** Experimental setup.

Considering a classic spring-damping-mass system, the system's model is following equation.

$$m\ddot{x} = mg - \xi\dot{x} - kx, \quad (8)$$

where $x$ is the position of mass dot, $g$ is gravitational acceleration, $\xi$ is damping ratio, and $k$ is the spring constant. Compare this equation to the third equation of the previous state space equation set, one can see that the DE membrane serves as the spring and damping components, assuming the DE actuator can be approximate as damping-spring component, then the functions $r(R, t)$, $\theta(R, t)$, and $\lambda_1(R, t)$, should also related to the state variables $x_1$, $x_2$. Hence the shape-related functions should be rewritten as $r(R, x_1, x_2)$, $\theta(R, x_1, x_2)$, and $\lambda_1(R, x_1, x_2)$. These state variables are heavily coupled, finding the explicit relationship between the displacement $x_1$ and input voltage $u$ is extremely difficult. Hence the PDEs are not practical in model-based controller design. To obtain a practical model, in this paper, an empirical modeling approach was used to obtain a transfer function relating the actuator's output to the input voltage. Although obtaining a general purpose model is difficult, in this application, instead of performing large deformation, the actuator only needs to work near its equilibrium point, and the over all deformation is small. In this application there is no need to know the complete shape of the membrane, take $R = b$ as a particle which is very close to the membrane's outer edge. Then the state space model with reduced order is as below equation.

$$\begin{cases} \dot{x}_1 = x_2 \\ \dot{x}_2 = \frac{1}{m}(b\sin(\theta(b, x_1, x_2)) \\ \times\left(1 - \left(\frac{x_3 r(b, x_1, x_2)}{b}\right)^2\right)\lambda_1(b, x_1, x_2) \\ - \left(\frac{b}{r(b, x_1, x_2)}\right)^2 \frac{b\sin(\theta(b, x_1, x_2))}{\lambda_1^3(b, x_1, x_2)}\Bigg) \\ \dot{x}_3 = -\frac{1}{R_c C}x_3 - \frac{1}{R_c C}u \end{cases}. \quad (9)$$

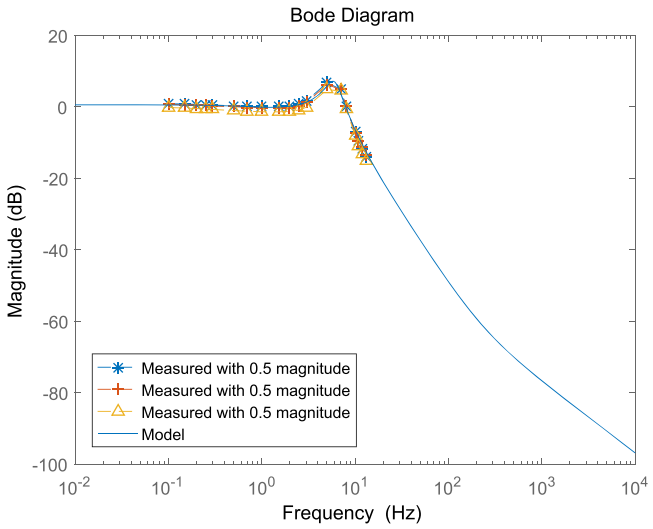


**Figure 7.** Bode plot of the system and its approximation with a nominal transfer function.

The equilibrium states can be obtained by putting a weight load on the central disk, and removing the input voltage. Wait until the disk reaches a static position, the equilibrium states are $x_1 = x_{01}$, $x_2 = x_{02}$, $x_3 = x_{03}$, $u = 0$, $r(R, x_{01}, x_{02})$, $\theta(R, x_{01}, x_{02})$, and $\lambda_1(R, x_0, x_{02})$. Then linearize the system near its equilibrium point, but the direct linearization result . The state-space equation is as follows:

$$\begin{cases} \Delta\dot{x}_1 = \Delta x_2 \\ \Delta\dot{x}_2 = f_1\Delta x_1 + f_2\Delta x_2 + f_3\Delta x_3, \\ \Delta\dot{x}_3 = -\frac{1}{R_cC}\Delta x_3 + \frac{1}{R_cC}\Delta u \end{cases} \tag{10}$$

where

$$\begin{aligned} f_1 = \; & \frac{1}{m}\Big(b\lambda_1\cos(\theta)\frac{\partial\theta}{\partial x_1} + b\sin(\theta)\frac{\partial\lambda_1}{\partial x_1} \\ & - \frac{x_3^2r^2\lambda_1}{b}\cos(\theta)\frac{\partial\theta}{\partial x_1} - \frac{x_3^2r^2}{b}\sin(\theta)\frac{\partial\lambda_1}{\partial x_1} \\ & - \frac{2rx_3^2}{b}\frac{\partial r}{\partial x_1} - \frac{b^3}{r^2\lambda_1^3}\cos(\theta)\frac{\partial\theta}{\partial x_1} \\ & + \frac{2b^3}{r^3\lambda_1^3}\sin(\theta)\frac{\partial r}{\partial x_1} + \frac{3b^3}{r^2\lambda_1^4}\frac{\partial\theta}{\partial x_1}\Big)_{x_1=x_{01},x_2=x_{02}}, \end{aligned} \tag{11}$$

$$\begin{aligned} f_2 = \; & \frac{1}{m}\Big(b\lambda_1\cos(\theta)\frac{\partial\theta}{\partial x_2} + b\sin(\theta)\frac{\partial\lambda_1}{\partial x_2} \\ & - \frac{x_3^2r^2\lambda_1}{b}\cos(\theta)\frac{\partial\theta}{\partial x_2} - \frac{x_3^2r^2}{b}\sin(\theta)\frac{\partial\lambda_1}{\partial x_2} \\ & - \frac{2rx_3^2}{b}\frac{\partial r}{\partial x_2} - \frac{b^3}{r^2\lambda_1^3}\cos(\theta)\frac{\partial\theta}{\partial x_2} \\ & + \frac{2b^3}{r^3\lambda_1^3}\sin(\theta)\frac{\partial r}{\partial x_2} + \frac{3b^3}{r^2\lambda_1^4}\frac{\partial\theta}{\partial x_2}\Big)_{x_1=x_{01},x_2=x_{02}} \end{aligned} \tag{12}$$

and

$$f_3 = -\frac{2r^2\lambda_1}{m}\sin(\theta)|_{x_1=x_{01},x_2=x_{02}}. \tag{13}$$

Hence the system's linearization model is a third-order system, and the state $x_1$, $x_2$ are heavily coupled with the membrane's shape. But it can be seen that the equation relating to $\Delta x_2$ is in the form of a typical damping-spring system's equation, $f_1$ serves as a spring constant, $f_2$ serves as a damping ratio, and $f_3$ is a gain of input. Then the equations relating to $\Delta\dot{x}_1$ and $\Delta\dot{x}_2$ form as a second-order system, which is using $\Delta x_3$ as input. The equation showing $\Delta\dot{x}_3$ is a first-order system, which presents the circuit model.

The frequency response of the actuator was needed to identify the parameters in the transfer function. Figure 6 shows the experimental setup for actuation test which measured the frequency response of the DE actuator. A 100 g weight load was put on the covering plate, and a Baumer OADM 20I6441/S14F laser displacement sensor was used to measure the weight load's movement. The measurement range of this distance sensor was 30–70 mm, good enough for the experiments. The diaphragm was connected to a high-voltage amplifier (5HVA24-BP1-F, UltraVolt Inc.), which was capable of outputting up to 5000 V This high voltage satisfied the driving voltage requirement of the diaphragm actuator. The laser sensor was connected to a DS1104 dSPACE system for collecting the output data. The power supply was also connected to the dSpace system for controlling the voltage applied on the actuator and reading the current of charging and discharging on the device.

Took the $R_c$ and $C$ as one parameter $R_cC$. By measuring the membrane's voltage and current values, the parameter was measured as $R_cC = \frac{1}{0.0045}$. The transfer function of the circuit model was as following equation.

$$G_2(s) = \frac{1}{0.0045s + 1}. \tag{14}$$

The following steps were taken to obtain the frequency response of the actuator. The voltage range of the amplifier was normalized from 0 to 1, with 1 meaning a full 5 KV output. Sinusoidal signals of 0.2 magnitude with different frequencies were fed into the amplifier, and the response magnitudes were calculated through a fast Fourier transformation algorithm. The frequency sweep from 0.1 to 13 Hz so that the low frequency response has been tested to capture the viscous-elastic behavior of a VHB tape. The same procedure was repeated with 0.2, 0.4 and 0.5 input magnitudes. All the measured frequency response data were plotted in a bode plot. After obtaining the frequency responses, a third-order transfer function was used to approximate the magnitude response data points by minimizing the curve's mean square error between data points. Figure 7 shows the bode plot of the transfer function and experimental data. The transfer function obtained from these procedures was below equation.

$$G_1(s) = \frac{1}{s^2 + 15.96s + 1444}. \tag{15}$$

Hence the overall linearized transfer function was the following equation.

$$G(s) = \frac{1350.14}{0.0045s^3 + 1.07182s^2 + 22.458s + 1444}. \tag{16}$$

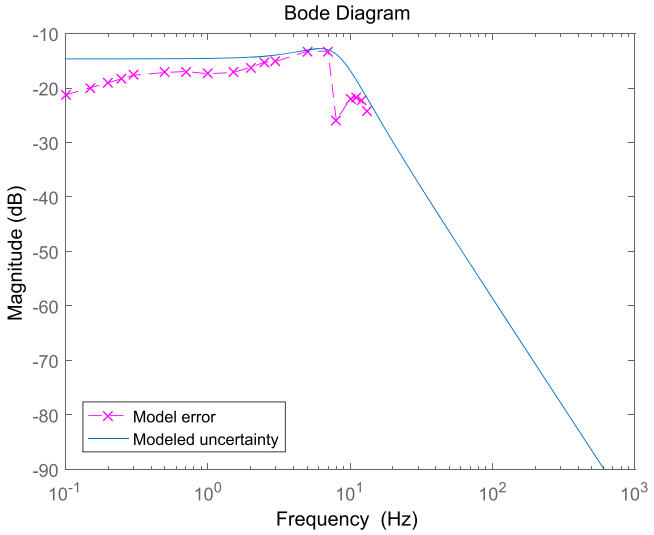


**Figure 8.** Model of the system's uncertainty.

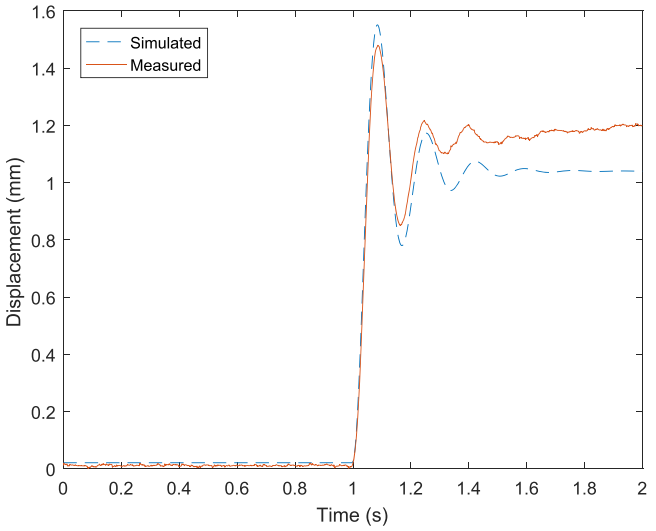


**Figure 9.** Displacement of the actuator under a 5 KV step voltage.

This black-box model captured the dynamics of the entire system, including dynamics of the controller, amplifier, and actuator. In order to estimate the modeling error, all absolute magnitude errors between the experimental data and the simulated data were plotted out in a Bode plot (figure 8). Then a second-order transfer function $W_s(s)$ was used to cap the magnitude of the modeling errors. In other words, $W_s(s)$, a bound of the system's uncertainty, was obtained. Hence, the $W_s(s)$ was

$$W_s(s) = \frac{487.5}{s^2 + 45s + 2500}. \tag{17}$$

The H-infinity norm of $W_s(s)$ will be used in the internal stability analysis in section 4.

To verify the nominal model (16), a step response under 5 KV was measured. Figure 9 shows that under a 5 KV step voltage, a 2 mm (approximate 4% of strain in terms of radius change) displacement was achieved with less than 0.5 s settling time. The step response curve of the diaphragm was similar to the step response of an under-damped second-order system. From figure 7, the natural frequency of the second order system was measured at 40 rad $s^{-1}$. Since the diaphragm actuator was more like a spring-mass system, the natural frequency can be described by

$$f = \frac{1}{2\pi}\sqrt{k/m}, \tag{18}$$

where $k$ is the spring constant of the diaphragm actuator, and $m$ is the mass of the load. From equation (18), $m = 0.1$ kg, and $f = 40/(2\pi)$ Hz, the spring constant can be calculated as $k = 160$ N $m^{-1}$. Based on the identified empirical model (16), a step response was simulated and plotted in figure 9 showing that the model can predict the step response of the actuator, and the average error between measured values and simulation results at steady-state was 6.91%, the steady state error is relatively large due to the model error. Since the approximated model ignores the actuator's visco-elasticity, when the input lasts for a period, the actuator will further displace for a small distance.

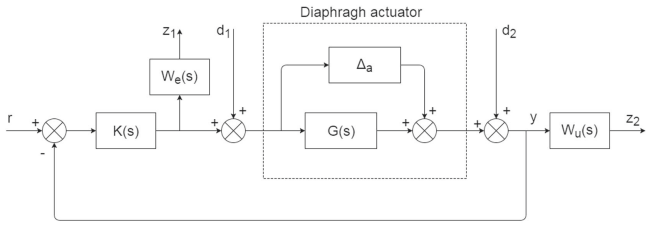


**Figure 10.** Block diagram of the control system.

## 4. H-infinity control design

The major challenge of the controller design is to track a multi-frequency reference with consideration of sensing noises, disturbances, and systems uncertainty. The reason that the authors choose H-infinity control is that H-infinity is robust to sensing noises, disturbance, and systems uncertainty [25]. In this paper, a standard H-infinity control design approach [25] was used to design a robust control of the DE actuator. As shown in section 3, a linear model was used to approximate the dynamics of the DE actuator, the system's uncertainty can not be avoided due to the nonlinear elasticity of soft material and un-modeled dynamics. When designing a robust control for the actuator, the system's uncertainty must be considered to ensure the internal stability of the system. Consider the system's block diagram as shown in figure 10, where $G(s)$ is the nominal plant of the system. $\Delta_a$ is an additive uncertainty, which is defined as the error between the response magnitudes of the nominal plant and the measured values; and signal $d_1$ denotes the disturbance and $d_2$ denotes the sensing noise. To evaluate the robustness of the controller, two artificial outputs $z_1$ and $z_2$ are added into the system and two performance

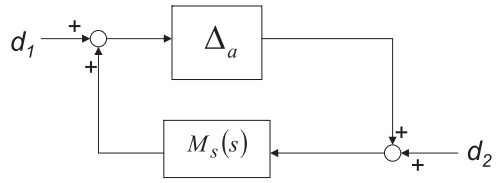


**Figure 11.** The feedback connection of $M_s(s)$ and $\Delta_a(s)$.

weights $W_u(s)$ $W_e(s)$ are associated with them, respectively [25]. $z_1$ and $W_e(s)$ are used to evaluate the control effort while $z_2$ and $W_u(s)$ are used to evaluate the tracking performance. The H-infinity controller $K(s)$ is designed to minimize the H-infinity norm of the transfer function from $[d_1, d_2]$ to $[z_1, z_2]$, thus the H-infinity control can minimize the impact of the sensing noise and disturbance on the tracking performance and control effort. Based on the design rule of H-infinity control [25], the weight functions of $W_u(s)$ and $W_e(s)$ were chosen as

$$W_u(s) = \frac{0.1s + 0.0006283}{0.0001s + 62.83}, \tag{19}$$

$$W_e(s) = \frac{0.2s + 6.283}{s + 0.0006283}. \tag{20}$$

By using the hinfsyn function in Matlab, the designed H-infinity controller was obtained as

$$K(s) = \frac{30.4975s^2 + 1232.4466s + 81241.5075}{s^3 + 17.5212s^2 + 5833.5515s + 3.6648}. \tag{21}$$

In order to analyze the system's internal stability with the controller $K(s)$ and system's uncertainty $\Delta_a(s)$, the control system shown in figure 10 can be redrawn as figure 11. The transfer function $M_s(s)$ can be written as

$$M_s(s) = \frac{K(s)}{1 + G(s)K(s)}. \tag{22}$$

Based on the small-gain theorem [25], in order to maintain the system's internal stability, the H-infinity norm of the system's transfer functions $M_s(s)$ and $\Delta_a(s)$ must satisfy the condition:

$$\|M_s(s)\|_\infty < \frac{1}{\|\Delta_a(s)\|_\infty}. \tag{23}$$

With (21), (16), and (22), one can calculate the H-infinity norm $\|M_s(s)\|_\infty = 1.7687$. The H-infinity norm of uncertainty $\|\Delta_a(s)\|_\infty < \|W_s(s)\|_\infty = 0.2426$. One can get

$$\|M_s(s)\|_\infty < \frac{1}{\|\Delta_a(s)\|_\infty} = 4.1218, \tag{24}$$

which satisfies the internal stability condition (23). The overall system's Bode plot is showing in figure 12. The system's response is relatively flat when its input frequency is lower than 6.07 Hz. One can see the system's response has a small drop when its input frequency increases close to

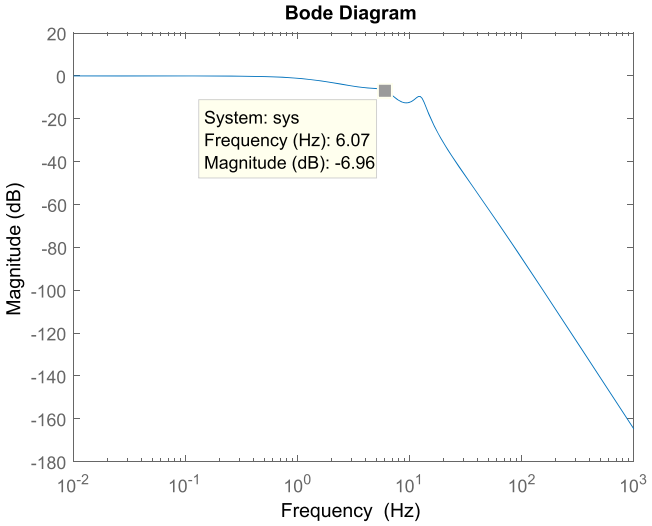


**Figure 12.** Bodeplot of over system.

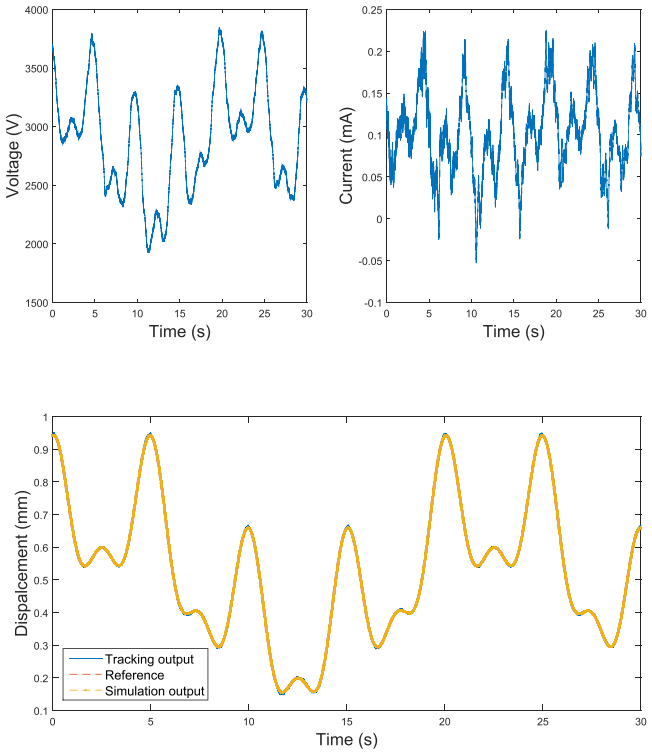


**Figure 13.** System's response with H-infinity controller.

6.07 Hz, which means the system has lower performance when input close to 6.07 Hz, then the system's response drops quickly. The selection of weighting transfer functions $W_e(s)$ and $W_u(s)$ affects the bandwidth of control system [25]. There is a trade-off between control effort and high frequency tracking performance. In this study, since the voltage applied to DE actuator should be smaller than 5 KV, $W_e(s)$ and $W_u(s)$ were selected so that the voltage did not

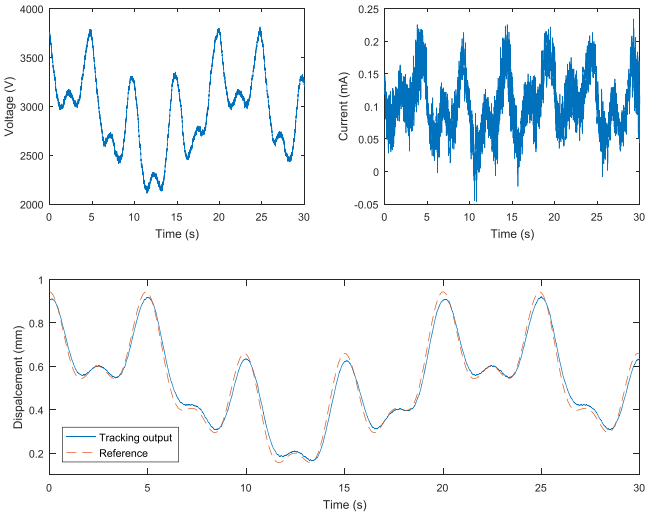


**Figure 14.** System's response with PID controller.

exceed 5 KV but the bandwidth of control system was limited to 6.07 Hz.

## 5. Experimental results

One goal of this research is using the actuator for the human pulse tracking purpose. Since The human pulse signal consists of multi-frequency components, in this section, the multi-frequency tracking performance and robustness of DE actuator is introduced first. Then the human pulse signal tracking is described second.

### *5.1. Multi-frequency reference tracking*

After the DE actuator and controller were ready for use, the first experiment was designed to verify the multi-frequency tracking capability and robustness of the controller. A multi-frequency reference signal was chosen to show the controller's tracking and noise-resistant capabilities. The reference signal was the sum of three sinusoidal waves:

$$r(t) = 0.2\sin(0.4\pi t + 1.5\pi) + 0.2\sin(0.1\pi t + \pi) + 0.1\sin(0.8\pi t + 0.5\pi). \quad (25)$$

To eliminate the noise in the laser sensor output, an additional low-pass filter was used:

$$G_{\text{fil}}(s) = \frac{40\pi}{s + 40\pi}. \quad (26)$$

Figure 13 shows the output response with the H-infinity controller. To show the control effort and power requirement, the mean square value of normalized voltage (linearly normalized form 0–5000 V into 0–1) was used as the control effort index, and the average power in a single input period was also calculated. The control effort for the H-infinity control was 0.3431. In a single period, the average power was 0.3186 W (negative current values were set to 0 since there was no power recycling, which was applied to all power measurement results in this paper). The average tracking error level was 0.0107 mm, which was 2.15% of the maximum reference magnitude.

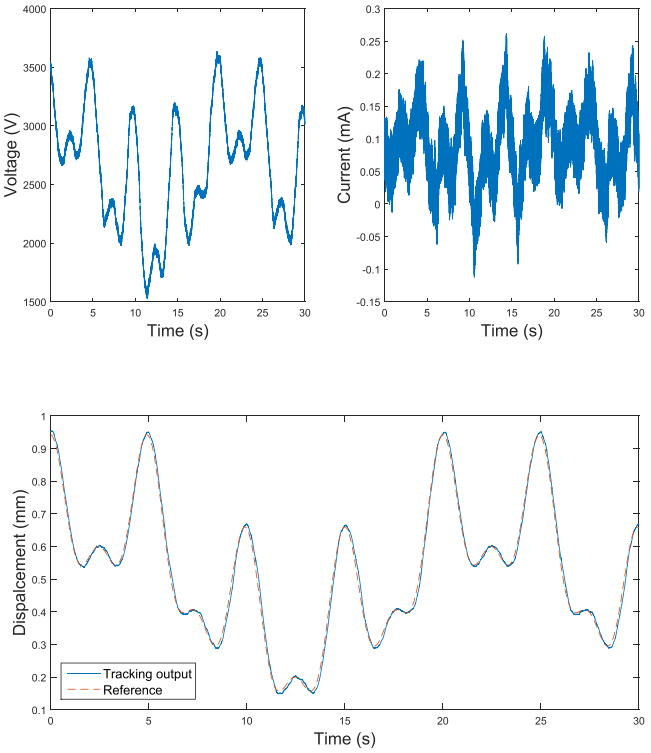


**Figure 15.** System response with the H-infinity controller after adding a constant disturbance and sensing noise.

**Table 1.** Performance of H-infinity Control.

| | Average error (mm) | Control effort index | Average power (Watt) |
|---|---|---|---|
| Normal | 0.0107 (2.15%) | 0.3431 | 0.3186 |
| Constant disturbance | 0.0114 (2.28%) | 0.3008 | 0.2678 |
| Sensing noise | 0.0107 (2.13%) | 0.3565 | 0.3355 |
| Disturbance noise | 0.0117 (2.34%) | 0.2935 | 0.2589 |

In comparison, an auto tuned PID controller was tested in this system. The PID controller's parameters were tuned in Matlab, which were $P = 3.1738$, $I = 48.6620$, $D = 0.0443$, and $N = 9630.0667$. However, the PID controller could not provide enough robustness, due to the system uncertainty and measuring noise, the system lost its stability in the experiment. A manually tuned PID controller requires lost of experiences and time to achieve the similar performance. For a quick comparison, the PID controller's parameters were set manually, where $P = 1.7$, $I = 24.331$, and $D = 0$, and $N = 9630.0667$ the tracking result of the PID controller is showing in figure 14.

A high frequency sensing noise, $d_1(t) = 0.02\sin(100\pi t)$ was added on the sensing channel. The disturbance made the

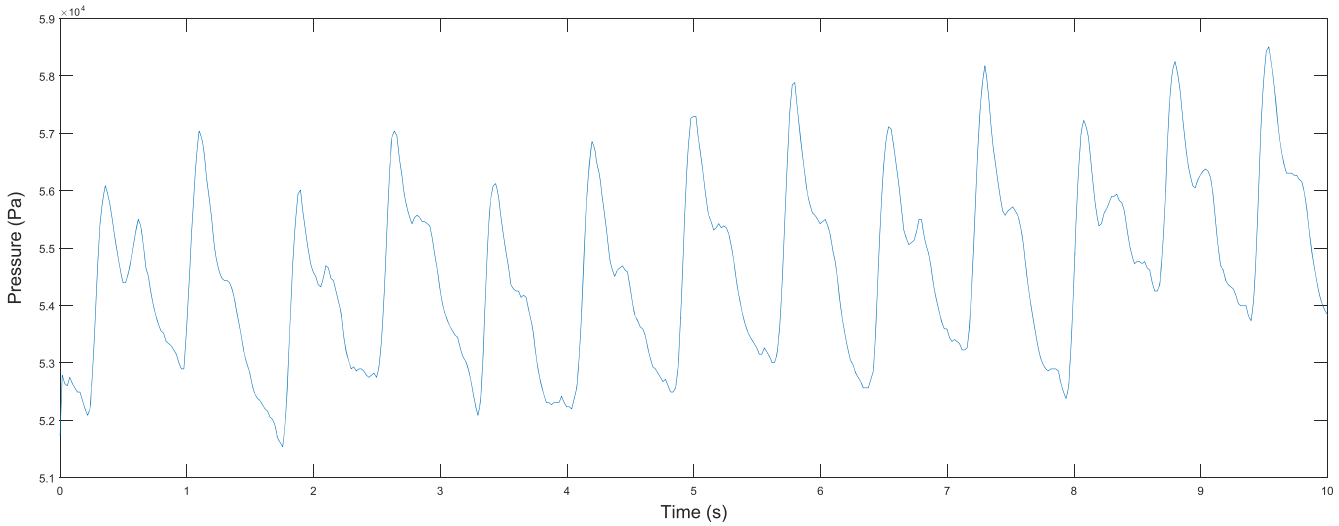


**Figure 16.** Measured human pulse from the Cun location on the wrist of a healthy man by the palpation robotic hand (PRH) developed by Dr Ho-Yin Chan at the City University of Hong Kong.

increase of the control effort and the error level, which were 0.3565 (average 0.3355 W in a single period) and 0.0107 (2.13%) for the H-infinity controller.

Figure 15 shows the output for the H-infinity controller with both sensing noise and a constant disturbance. With the H-infinity controller, an error level of 0.0117 mm was obtained, or 2.34% of the reference magnitude, while the control effort was about 0.2935, with the average of 0.2589 W in a single period. Since the H-infinity controller optimally filtered out the disturbance signal and sensing noise in the control output, the H-infinity controller reduced the effect of disturbance and noise on the output. In summary, the average error, control effort, and power of the H-infinity controller under different conditions are showed in table 1.

### *5.2. Human pulse signal tracking*

As the first application, the DE diaphragm actuator was applied to track a human pulse pressure. A medical device developed by Lee and Chan [8] was used to collect human pulse pressure signals at the City University of Hong Kong. In one embodiment, the device included a robotic finger comprising a humanoid-finger structure, and a membrane for transferring an actuating force to the structure at an actuation point thereon and along an actuation direction. One end of the structure was mounted to a fulcrum, and another end had a sensing area. The robotic finger was configured such that, when the sensing area contacted a person's wrist, a first perpendicular distance from the fulcrum to a first line was substantially longer than a second perpendicular distance from the fulcrum to a second line, where the first line was a straight line passing through a sensing point of the sensing area and substantially perpendicular to the sensing area, and the second line was a straight line passing through the actuation point and oriented along the actuation direction. Figure 16 shows a human pulse pressure from the Cun location of a healthy person, and figure 17 shows the spectrum of the pulses.

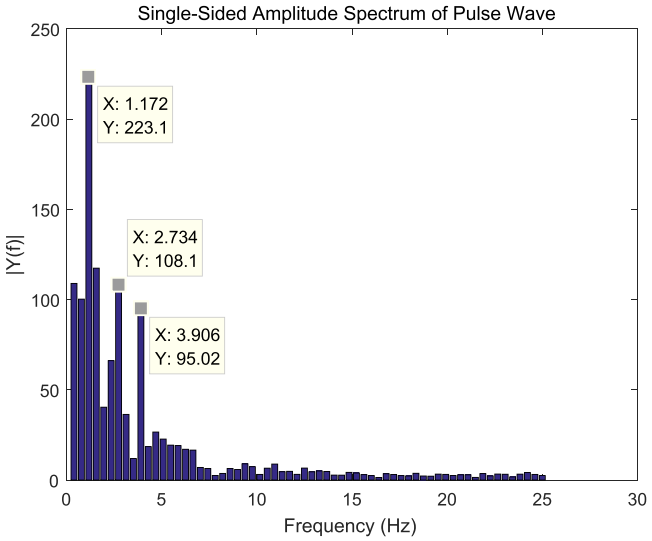


**Figure 17.** Spectrum of the human pulse signal.

From the human pulse signal shown in figure 16, it can be seen that the peak-to-peak pressure difference of pulse signal was 827.3709 Pa. From the spectrum of the pulse (figure 17), the fundamental frequency was 1.172 Hz, the second mode harmonic frequency was 2.734 Hz, and the third-mode harmonic frequency was about 3.906 Hz. In figure 7, the cut-off frequency of the DE actuator was 8 Hz, which means that, theoretically, the DE actuator is capable of tracking human pulse in terms of matching its up-to fifth-mode harmonic frequency components.

The human pulse pressure signal was then sent to WSU in the US through the Internet. To replicate the pulse signal, one should first convert the pressure signal in Pascal to the displacement in mm since the actuator's output was displacement. In section 3, the measured spring constant was $k = 160\ \mathrm{N\,m^{-1}}$, and the area of the small plate was $S = \pi r^2$, where $r = 6.35$ mm. The equivalent pressure, which could generate a 1 mm displacement, was calculated

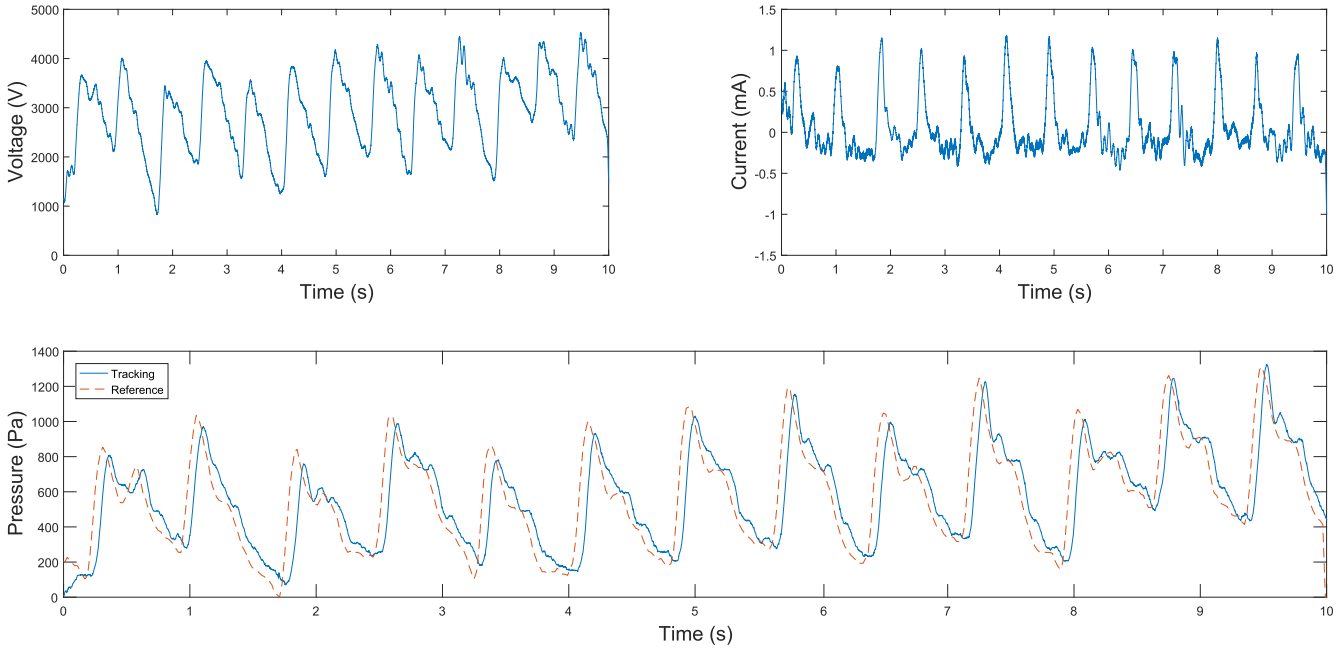


**Figure 18.** Tracking of the human pulse signal.

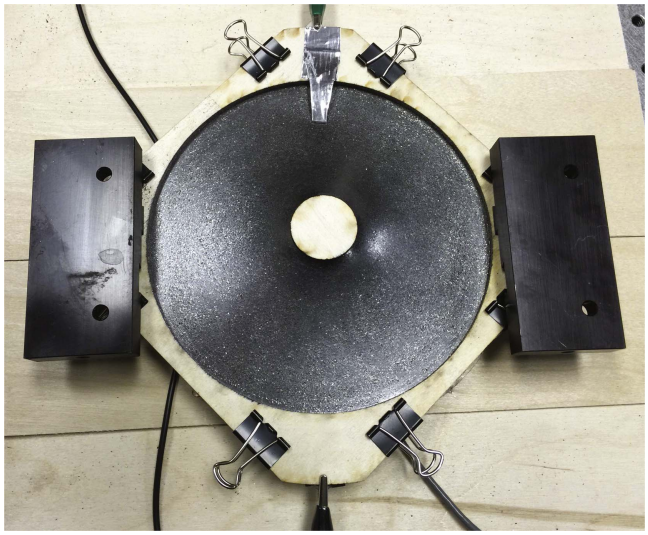

**Figure 19.** Experimental setup of the test with force sensing feedback control.

as 1296.2144 Pa mm$^{-1}$. Since the peak-to-peak of the human pulse pressure was 841.16039 Pa and the actuator was able to generate up to 1 mm displacement (figure 13), it could be concluded that the actuator was capable of tracking human pulse signal in terms of matching its magnitude. In the real-time implementation, the pulse signal was converted into a reference signal in displacement and then put into the dSpace system. Figure 18 shows the results of tracking a real human pulse pressure. The output pressure tracked the pulse signal well for its low-frequency components but with some small tracking errors for its high-frequency components, and there was a small time shift of nearly 40 ms. The voltage output was less than 5 KV, which verified that the DE material was safe under that voltage. Experimental results have shown that the DE actuator with its robust control was capable of tracking the human pulse pressure signal.

### *5.3. Pressure tracking of human pulse using force sensing feedback control*

This actuator was able to output displacement value as a demonstration of the capability of DE actuator. Further an experiment with force sensing feedback control was designed to make the actuator output track the pressure value. By replacing the weight load with a load cell, and let the load cell to push the central disk down. Figure 19 shows the experimental setup for the test with force sensing feedback control. The diaphragm was pre-deformed by a load cell (GS0-250, Transducer Techniques, LLC), which was installed under the central plate. The actuator was pushed by the load cell, and the pressure change could be also measured by the load cell. With the same human pulse signal, the actuator's pressure output was showing in figure 20. In this working mode, one can see the actuator was not affected by the inertia of weight load, the delay time in response was less than former result. The actuator's response followed the reference at the beginning jump of the input, which was lost in the displacement tracking mode. Moreover, the small vibration in the reference wave was approximated better in pressure tracking mode, this means the actuator could reflect more details of the human pulse signal.

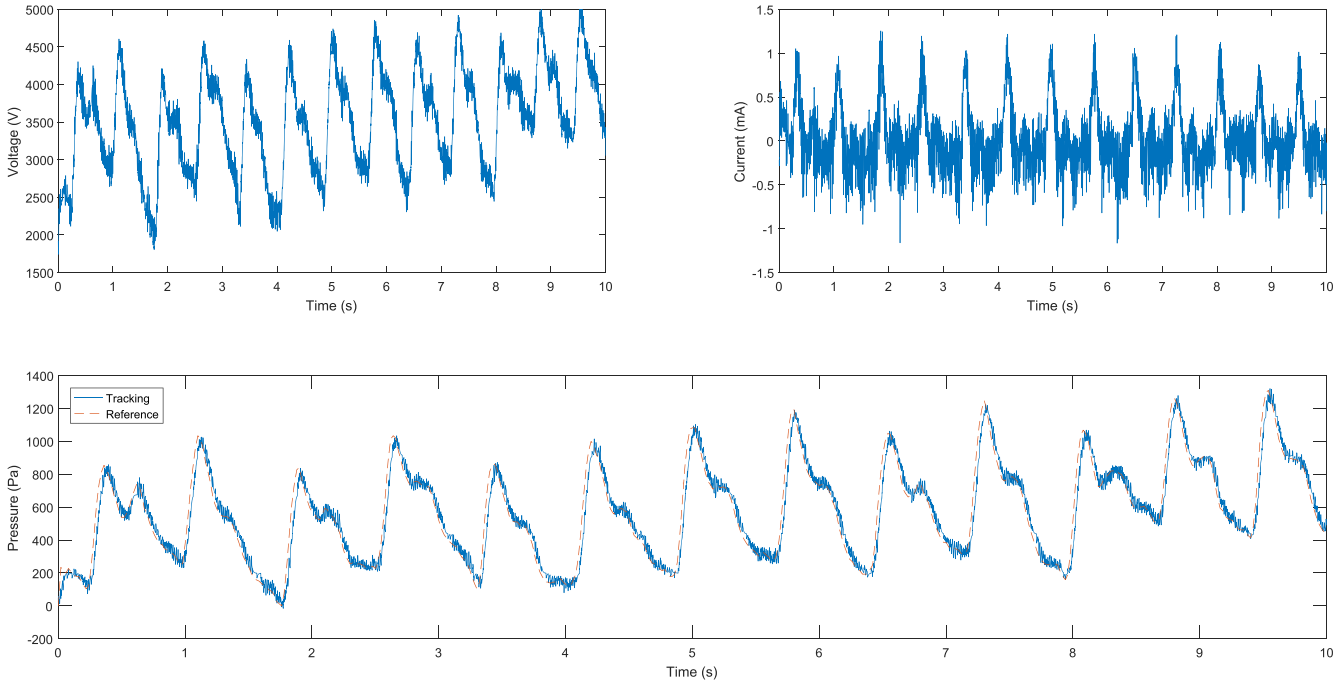


**Figure 20.** Pressure tracking of the human pulse signal.

## 6. Conclusions and future work

In this paper, a diaphragm actuator of DE was designed and fabricated for human pulse signal tracking. A physical model was developed to capture the dynamics of the actuator, and then an H-infinity controller was built for the actuator based on the physical model. Experimental results have shown that the H-infinity controller was capable of controlling the actuator to track a multi-frequency reference signal with existence of sensing noises, disturbances, and uncertainties. A set of human pulse pressure signals were measured in Hong Kong and replicated by the DE actuator in the US. Experimental results have shown that the DE actuator with H-infinity control was capable of tracking the human pulse pressure signals.

Considering the actuator's compliant structure and capability of accurate deformation, DE actuators will be ideal to replicate the movement of biological tissues or organs. Our future work will focus on developing a human pulse signal tracking device for traditional Chinese medicine. The actuator's time-varying property will remain a problem, calling for an adaptive control. How to obtain a larger deformation and avoid multiple types of material failure will also be interesting research directions. In the future work, a Chinese traditional medical doctor will participate in double-blind studies of telediagnosis to test this device.

## Acknowledgments

This research was supported in part by the National Science Foundation under CAREER Grant DCSD #1653301 and the Kansas Engineering Expansion Grant: House Substitute for Substitute Senate Bill No. 127, an act Enacting the University Engineering Initiative Act. The authors would like to thank Mr Ka Wai Hong at the City University of Hong Kong for collecting human pulse data.

## ORCID

Zheng Chen https://orcid.org/0000-0002-5339-7596

## References

[1] Lenoble P, Kheliouen M, Bourderont D, Klinger V, Nasica X, Benseddik Y and Holl P 2009 Screening diabetic retinopathy using a telediagnosis system. Results of the upper rhine survey *J. Fr. d'Ophtalmologie* **32** 91–7

[2] Setyono A, Alam M J and Eswaran C 2014 Mobile telemedicine system application for telediagnosis using multimedia messaging service technology *Int. J. Wirel. Mobile Comput.* **7** 348

[3] Hishitani T, Fujimoto Y, Saito Y, Sugamoto K, Hoshino K and Ogawa K 2014 Accuracy of telediagnosis of fetal heart disease using ultrasound images transmitted via the internet *Pediatrics Int.* **56** 289–91

[4] Kassaba R, Lapayrea J-C, Aupeta J-B, Marzanib F and Pierallia C 2013 Scars collaborative telediagnosis platform using adaptive image flow *Integr. Comput.-Aided Eng.* **20** 3–14

[5] Brunetti N, Dellegrottaglie G, De Gennaro L and Di Biase M 2015 Original article/telediagnosis: Telemedicine pre-hospital electrocardiogram for acute cardiovascular disease management in detainees: an update *Eur. Res. Telemed./La Recherche Européenne en Télémédecine* **4** 25–32

[6] Hishitani T, Fujimoto Y, Saito Y, Sugamoto K, Hoshino K and Ogawa K 2014 A medical link between local maternity hospitals and a tertiary center using telediagnosis with fetal cardiac ultrasound image transmission *Pediatric Cardiol.* **35** 652

[7] Wang H and Cheng Y 2006 A quantitative system for pulse diagnosis in traditional Chinese medicine *Proc. 27th Annual Int. Conf. of the Engineering in Medicine and Biology Society* pp 5676–9
[8] Lee F and Chan H 2014 Methods and device for sensing a person's pulse in traditional chinese medicine *US Patent* US20 140 323 886 A1
[9] Pelrine R, Kornbluh R, Joseph J, Heydt R, Pei Q and Chiba S 2000 High-field deformation of elastomeric dielectrics for actuators *Mater. Sci. Eng.* C **11** 89–100
[10] Chuc N H, Vuong N H L, Kim D S, Moon H P, Koo J C, Lee Y K, Nam J-D and Choi H R 2011 Fabrication and control of rectilinear artificial muscle actuator *IEEE/ASME Trans. Mechatronics* **16** 167–76
[11] Suo Z 2010 Theory of dielectric elastomers *Acta Mech. Solida Sin.* **23** 549–78
[12] Pelrine R, Kornbluh R, Pei Q and Joseph J 2000 High-speed electrically actuated elastomer with strain greater than 100% *Science* **287** 836–9
[13] Foo C C, Cai S, Koh S J A, Bauer S and Suo Z 2012 Model of dissipative dielectric elastomers *J. Appl. Phys.* **111** 034102
[14] He T, Cui L, Chen C and Suo Z 2010 Nonlinear deformation analysis of a dielectric elastomer membrane-spring system *Smart Mater. Struct.* **19** 085017
[15] Ye Z, Faisal M S S, Asmatulu R and Chen Z 2014 Artificial muscles of dielectric elastomers attached to artificial tendons of functionalized carbon fibers *Proc. SPIE* **9056** 905616
[16] Ye Z, Faisal M S S, Asmatulu R and Chen Z 2015 Bio-inspired artificial muscle structure for integrated sensing and actuation *Proc. SPIE* **9430** 943024
[17] Faisal M S S, Ye Z, Chen Z and Asmatulu R 2015 Electrical properties of nanoscale metallic thin films on dielectric elastomer at various strain rates *Proc. SPIE* **9430** 943031
[18] Plante J-S 2006 Dielectric elastomer actuators for binary robotics and mechatronics *PhD Dissertation* Massachusetts Institute of Technology
[19] Pelrine R, Sommer-Larsen P, Kornbluh R D, Heydt R, Kofod G, Pei Q and Gravesen P 2001 Applications of dielectric elastomer actuators *Proc. SPIE* **4329** 335
[20] Vertechy R, Bergamasco M, Berselli G, Castelli V P and Vassura G 2013 Compliant actuation based on dielectric elastomers for a force-feedback device: modeling and experimental evaluation *Frattura e Integrita Strutturale* **23** 47–56
[21] Xie S Q, Ramson P, Graaf D, Calius E and Anderson I A 2005 An adaptive control system for dielectric elastomers *IEEE Int. Conf. on Industrial Technology, 2005. ICIT 2005* (Piscataway, NJ: IEEE) pp (doi:10.1109/ICIT.2005.1600660)
[22] Toth L A and Goldenberg A A 2002 Control system design for a dielectric elastomer actuator: the sensory subsystem *Proc. SPIE* **4695** 323
[23] Jiang C, Takagi K, Suzuki T, Hosoe S, Nozawa A and Hashimoto K 2013 Experimental study of position control with tube-type dielectric elastomer actuator *2013 Int. Conf. on Advanced Mechatronic Systems (ICAMechS)* (Piscataway, NJ: IEEE) pp 352–6
[24] Rizzello G, Naso D, Turchiano B and Seelecke S 2016 Robust position control of dielectric elastomer actuators based on lmi optimization *IEEE Trans. Control Syst. Technol.* **24** 1909–21
[25] Zhou K and Doyle J C 1998 *Essentials of Robust Control* (Upper Saddle River, NJ: Prentice-Hall)